Journal of Engineering Mathematics **37:** 253–272, 2000.

Cagniard-de Hoop path perturbations with applications to nongeometric wave arrivals

D. P. WILLIAMS[1] and R. V. CRASTER[2]
[1]*Division of Theoretical Mechanics, School of Mathematical Sciences, University of Nottingham, Nottingham, NG7 2RD, U.K.*
[2]*Department of Mathematics, Imperial College of Science, Technology and Medicine, London, SW7 2BZ, U.K.*

Received 24 September 1998; accepted in revised form 4 May 1999

Abstract. Nongeometric wave arrivals are often important in seismology and elastic wave studies related to the nondestructive evaluation of structures. In particular, tunnelling signals caused by significant differences in the material parameters, and wavespeeds at interfaces, generate large responses that may often be dominant. This is common in elastic wave propagation, for instance, when a source is close to the interface of a faster medium with a slower medium, the response in the slower medium is dominated by a signal that has *tunnelled* through the faster medium. Other instances of tunnelling occur when a compressional source is close to a free surface. In this case the compressional to shear wave conversion at the surface, and the mismatch between compressional and shear wavespeeds, leads to a sharp nongeometric shear wave arrival. Equally, thin high velocity layers demonstrate tunnelling effects that are perturbations of the response brought about by a source in a surrounding slower medium. In the above *close* refers to the viewpoint of an observer some distance away. In all of the instances there is a common feature, namely, each problem contains a ratio of length scales, x/h, with h either the source depth or layer thickness and x the observer distance; this ratio of length scales characterises the nongeometric responses. Typically, the nongeometric response arises when the current problem is a perturbation away from one where the associated arrival has a direct geometric interpretation.

Such problems are ideally suited to analysis by the Cagniard-de Hoop technique. Each tunnelling response is identified as a perturbation away from an exact solution; this leads to highly accurate and relatively simple explicit asymptotic solutions. The perturbation scheme is demonstrated here via the solution of two problems: a compressional source beneath a fluid-solid interface and beneath a thin high velocity layer. The first problem has separate nongeometric responses due to both the material mismatch and the wave conversion at the interface. The thin high velocity layer perturbs the field generated by a compressional source in a slower surrounding medium. In both cases the nongeometric arrivals are analysed in detail.

Key words: elastic waves, tunnelling, interface, layer.

1. Introduction

The Cagniard-de Hoop technique, Cagniard [1], de Hoop [2], provides an excellent method for solving and investigating various elastic wave interaction problems. Indeed, many model problems can be analysed in detail, and both the physical structure and the importance of the responses determined. In particular, the interactions between source excitations, interfaces and layers are revealed, and explicit solutions found; this, together with a useful asymptotic scheme, is the aim of the current paper.

In seismology and seismic exploration many cases exist where tunnelling is important; this contribution is sometimes overlooked. One major area where this response is relevant is in oil exploration where shallow explosive sources generate these signals due to mode conversion

at the free surface. The responses may also be evident in acoustic microscopy when dealing with scattering by shallow sub-surface cracks.

The method itself is discussed in considerable detail by Aki and Richards [3], Miklowitz [4], and others. In essence, the solution is given in terms of a path (or several paths) $\zeta(x, y, t)$ that, in general, depends on a parameter, h, that is either the source depth, or the layer thickness. Using a particular time dependence the Cagniard–de Hoop method consists of an elegant transformation that reduces a double transform inversion to an explicit result; more general time dependence is then easily incorporated using convolution theorems.

In brief, we utilise Fourier and Laplace transforms in space and time respectively: the Laplace transform in time t, and its inverse, are defined as

$$\overline{f}(p) = \int_0^\infty f(t)\mathrm{e}^{-pt}\mathrm{d}t, \qquad f(t) = \frac{1}{2\pi\mathrm{i}}\int_{c-\mathrm{i}\infty}^{c+\mathrm{i}\infty} \overline{f}(p)\mathrm{e}^{pt}\mathrm{d}p, \quad \text{for } \mathfrak{Re}(c) > 0 \tag{1.1}$$

where p is the Laplace transform variable, and the Fourier transform in x, and its inverse, are defined as

$$\widetilde{f}(\xi) = \int_{-\infty}^\infty f(x)\mathrm{e}^{\mathrm{i}\xi x}\mathrm{d}x, \qquad f(x) = \frac{1}{2\pi}\int_C \widetilde{f}(\xi)\mathrm{e}^{-\mathrm{i}\xi x}\mathrm{d}\xi, \tag{1.2}$$

where ξ is the Fourier transform variable. The inversion path C runs along the real axis from $-\infty$ to ∞. Using transformations of the governing equations, to be discussed in Section 2, and a rescaling of the transform variable, typically $\xi = p\zeta$, we obtain

$$f(x, y, t) = \frac{1}{2\pi\mathrm{i}}\int_{c-\mathrm{i}\infty}^{c+\mathrm{i}\infty} \frac{1}{2\pi}\int_{-\infty}^\infty g(\zeta)\mathrm{e}^{-pz(\zeta)}\mathrm{d}\zeta\,\mathrm{e}^{pt}\mathrm{d}p. \tag{1.3}$$

Both the functions $g(\zeta)$ and $z(\zeta)$ are usually rather complicated, containing branch points and poles. Typically, as in the case we consider in Section 2, the function $z(\zeta)$ takes the form

$$z(\zeta) = \gamma_d(\zeta)h + \gamma_s(\zeta)y + \mathrm{i}\zeta x. \tag{1.4}$$

The functions γ_q that appear are defined as $\gamma_d(\zeta) = (\zeta^2 + 1)^{1/2}$, $\gamma_s(\zeta) = (\zeta^2 + k^2)^{1/2}$, where the branch cuts are taken running along the imaginary axes from $\pm\mathrm{i}$ to $\pm\mathrm{i}\infty$ and $\pm\mathrm{i}k$ to $\pm\mathrm{i}\infty$ respectively. The Cagniard-de Hoop technique now involves defining a Fourier inversion path $\zeta(x, y, t)$ such that it is the solution of the transcendental equation $z(\zeta) = t$, namely

$$t = \gamma_d(\zeta)h + \gamma_s(\zeta)y + \mathrm{i}\zeta x, \tag{1.5}$$

with $t > t_{\text{critical}}$ say. Once such a path is found the double transform above becomes the inverse Laplace transform of a Laplace transform, thus the explicit answer is clear by inspection.

In simple cases when, say $h = 0$, Equation (1.5) is solvable explicitly and this then yields much useful information. In particular we can study the wavefront arrivals and their asymptotic forms explicitly. These can then be used in conjunction with a convolution theorem to generate fast and accurate artificial seismograms.

The limit as the ratio $h/x \to 0$ is of interest in many applications. This perturbation away from $h = 0$ smooths out the sharp wavefront arrivals that were, when $h = 0$, associated with saddle points in the transform domain, or equivalently specific points on the Cagniard paths

where the path left the branch cuts. Once the parameter h is nonzero the analysis becomes more difficult since the path $\zeta(t)$ must now be found numerically. A quartic equation may be formulated and solved explicitly see Williams [5], however in the limit as $h \to 0$ this is not particularly revealing. In this case we expect the asymptotics of the wavefronts to be less obvious; this occurs for many model problems. For instance the path in (1.5) is required if we are interested in studying the $S^\star$ arrival, Hron and Mikhailenko [6], that has been given much attention and which we describe in Section 2. In the limit as the source tends to the interface, $h \to 0$, the Cagniard path has a noticeable sharp bend; this has been noticed before by Hron and Mikhailenko [6]. This dramatic bend occurs near to the point at which the path would have left the branch cuts when $h = 0$, thus it is natural to investigate perturbing away from the $h = 0$ solutions.

In the case of a thin fast fluid layer sandwiched between larger fluid layers, Mellman and Helmberger [7] also noticed a sharp bend in one of the Cagniard paths for a generalised ray and drew attention to the connection with the non-geometric transmitted wavefront. Later Drijkoningen and Chapman [8] and Drijkoningen [9] suggested that this bend in the Cagniard path was generic for many wave arrivals of this type, and that the Cagniard technique was the natural way to study these phenomena. The problems treated in Drijkoningen and Chapman [8] concentrate upon fluid half spaces for which the Cagniard paths are known explicitly, the current paper is an extension of this approach in that the elastic counterparts are treated. More generally the perturbation scheme we use easily leads to asymptotic results in the more complicated cases when the Cagniard path must be found numerically.

One detail that appears to have been overlooked, but is rather useful, is that in the limit as the ratio h/x tends to zero we can use the explicit path found when $h = 0$ to generate an accurate asymptotic representation for $\zeta(t)$ outside some close neighbourhood of $t_{s^\star}$, that we discuss and determine in Section 2. In itself this is already faster than finding $\zeta(t)$ numerically but crucially any further manipulations are much less time-consuming, particularly if we then wish to look at quite general time dependent sources, or consider extensions to three dimensions. It also indicates that the approach might be equally rewarding in anisotropic media. More importantly it also allows a thorough asymptotic analysis of the underlying physical problems to be examined.

In this paper we consider a compressional source beneath a fluid-solid interface. This problem illustrates tunnelling effects within a *slow* material (the fluid) due to a source in a *fast* material, and also tunnelling in the *fast* material due to the coupling between a *fast* compressional wave and a *slow* shear wave.

To demonstrate the wider applicability of the approach used here we also consider a thin fast layer and use generalised ray theory to analyse this in detail. In this case we pick out the paths relating to the non-geometric arrivals, and these are then treated using the asymptotic approach.

Several alternative approaches to similar problems have been considered in the literature, but the explicit effect of the non-geometric waves is often hard to extract. Treating time harmonic dependence, several authors have identified high frequency, far field responses, see for instance Abramovici *et al.* [10], Gutowski *et al.* [11], Daley and Hron [12]; the analysis then involves steepest descents and follows, say, Brekhovskikh [13]; the equivalent responses are evanescent waves. Complex ray theory could also be employed since the arrivals have complex phase, see for instance Einziger and Felsen [14], Babich and Kiselev [15], or numerical modelling, see for instance Hron and Mikhailenko [6], Stephen and Bolmer [16]. However, the Cagniard-de Hoop approach is very direct, particularly revealing, and explicit solutions

in all space and time are deduced; the time harmonic results, if required, are then a subset of these solutions.

2. A compressional source beneath a fluid-solid interface

In this section we solve the problem of a compressional source beneath a fluid-solid interface. We demonstrate that, in the limit as the ratio $h/x \to 0$, a definite response occurs in the solid associated with the prominent $S^\star$ arrival. The $S^\star$ response is a non-geometric arrival that is formed by the reflected shear wave at the interface. Moreover, we identify the part of the Cagniard path that contributes to this response, namely the bend in the path that is close to the branch cuts. In order to appreciate the characteristics of the pseudo-shear wave a wavefront expansion is deduced using a perturbation of the Cagniard path that may be found explicitly when the source depth $h = 0$. This approach will open the way to considering a wide range of problems that contain a characteristic length scale h that effects non-geometric responses. In the next section we consider a thin fast layer; this configuration often occurs in model problems. The non-geometric response in the fluid is not treated here.

The fluid-solid configuration to be considered is shown in Figures 1 and 2 with the y-axis pointing downwards. The depth, h, of the line compressional source is not shown; it is taken to be $0 < h/x \ll 1$. In addition a schematic of the primary geometric wavefronts generated in each case, $h/x \to 0$ and $h = 0$, is shown in Figure 1 and Figure 2 respectively. Here the situation $h = 0$ is non-physical for the compressional source loading as it does not satisfy the interfacial conditions correctly. Nevertheless, the physical effects are relevant when this problem is perturbed; we are interested in this limiting case.

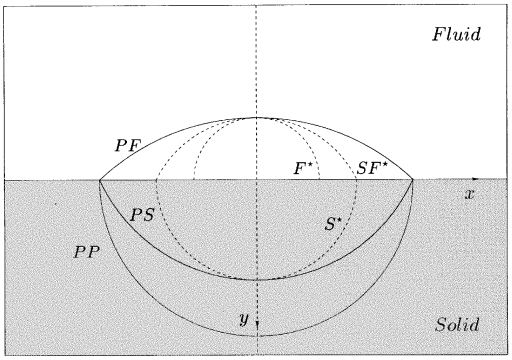

Figure 1. A schematic showing the radiated wavefronts for the waves generated by a line compressional source in the limit as the ratio $h/x \to 0$.

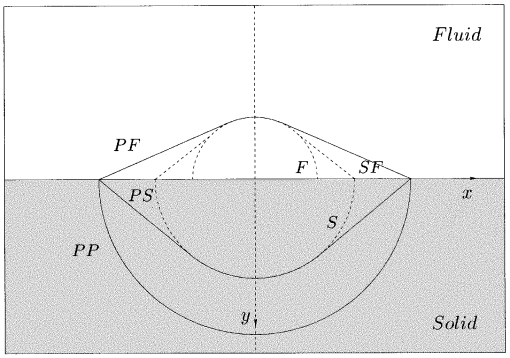

Figure 2. A schematic showing the radiated wavefronts for the waves generated by a line force at a fluid-solid interface; $h = 0$.

The notation that appears in the two schematics has been adopted from geometrical ray theory. The letters PP, PS, and PF are used to denote the compressional and shear waves in the solid, and the compressional wave in the fluid, generated by the direct compressional field

from the source respectively. In the case $h = 0$ both the PS and PF responses take the shape of head waves.

The starred letters $F^\star$, $S^\star$, and $SF^\star$ are used to denote the compressional wave in the fluid, the shear wave in the solid, and the head wave in the fluid generated by the shear wave respectively, in Figure 1. That is, these are the waves generated by interaction with the interface. These waves are the precursors to the unstarred field in Figure 2, and are investigated in the current paper. As h is sufficiently increased the starred fields loose their prominence. In addition, the figures omit the wavefronts due to the interfacial Schölte wave and, for light fluid loading, the leaky Rayleigh wave, and the direct compressional wave from the source.

The configuration consists of an isotropic linear elastic material in $y > 0$ and a compressible fluid in $y < 0$. The responses of the two half spaces are coupled together through the continuity boundary conditions along the interface $y = 0$, these are discussed following (2.1). A Cartesian coordinate system is adopted with $x_1,\ x_2$ corresponding to x, y.

In the usual way, the elastic material has Lamé constants $\lambda,\ \mu$, and density ρ. The stresses σ_{ij} in the material are related to the displacements u_i via $\sigma_{ij} = \lambda\varepsilon_{kk}\delta_{ij} + 2\mu\varepsilon_{ij}$ where $\varepsilon_{ij} = 1/2(u_{i,j} + u_{j,i})$, the comma denoting differentiation with respect to x_i. The governing equations in the elastic material are the equilibrium equations $\sigma_{ij,j} = \rho\ddot{u}_i$, where the notation $\ddot{}$ denotes double differentiation with respect to time.

The compressible fluid in $y < 0$ is effectively an elastic material that supports no shear stresses. Thus $\sigma_{ij} = \lambda_f\varepsilon_{kk}\delta_{ij}$, where the fluid has density ρ_f and compressional modulus λ_f. The governing equations are $\sigma_{ij,j} = \rho_f\ddot{u}_i$ again.

We utilise the displacement potentials ϕ, ψ, and χ where the displacements are $\mathbf{u} = \nabla\phi + \nabla \times \psi\hat{z}$ (where $\hat{z}$ is the unit vector in the z direction) in $y > 0$ and $\mathbf{u} = \nabla\chi$ in $y < 0$. The displacement potentials ϕ and ψ are related to the compressional and shear disturbances respectively, thus we utilise these when generating compressional sources. The following wave speeds c_d, c_s, and c_o are defined in terms of the material parameters as $c_d^2 = (\lambda+2\mu)/\rho$, $c_s^2 = \mu/\rho$, and $c_o^2 = \lambda_f/\rho_f$.

The assumption that the compressional wavespeed of the fluid is less than the shear wavespeed of the solid is taken so that $c_d > c_s > c_o$; this is a reasonable assumption for most solid and fluid combinations. The analysis presented here does not rely on this assumption, and is easily generalised to allow $c_d > c_o > c_s$, say, which would be typical of perspex-water combinations. A coupling parameter ε occurs in the analysis; it is defined as $\varepsilon = \rho_f c_o/\rho c_d$, and gives a measure of the fluid-solid coupling. The light fluid loading limit is when $\varepsilon \ll 1$; this specific limit is not taken here unless explicitly stated.

The continuity boundary conditions

$$[\sigma_{yy}(x, 0, t)] = 0, \qquad \sigma_{xy} = 0, \qquad [u_y(x, 0, t)] = 0 \tag{2.1}$$

are taken on the interface $y = 0$, where the braces [ ] denote the jump in a quantity across the interface; both the stresses σ_{yy} and the normal displacement u_y are continuous across $y = 0$. The fluid supports no shear stresses, thus $\sigma_{xy} = 0$ on $y = 0$. The total field in the solid consists of the superposition of two fields. The first is the solution to the source problem $\nabla^2\phi - \ddot{\phi}/c_d^2 = F(t)\delta(x)\delta(y - h)$, in an infinite elastic material, where $F(t)$ gives the time dependence of the source and $\delta(\ )$ denotes the delta function. The second field is the response generated by the interfacial boundary conditions; all figures show this second field.

The analysis is performed using the Fourier and Laplace transforms defined by Equations (1.1) and (1.2) respectively. The representations for the Fourier and Laplace transformed

stresses and displacements are given in Appendix A of Craster [17]; they are not repeated here.

The plan of this section is that we solve the source problems exactly, both for displacements and stresses; the asymptotic analysis is then developed as in Williams [5]. In this paper we concentrate solely upon the asymptotics associated with the non-geometric effect; the asymptotics for the other responses are shown in the figures, but the expressions are not given explicitly here. We concentrate upon the $S^\star$ response in the solid; the $F^\star$ response in the fluid is treated more briefly in Williams [5].

2.1. EXACT SOLUTION

Using the appropriate integral representations the solutions are derived. In the solid the Laplace transform of the normal displacement is

$$\begin{aligned}\overline{u}_y(x,y,p) &= -\frac{1}{2\pi}\int_{-\infty}^{\infty}\frac{1}{2c_d}\frac{p\overline{F}(p)s(\zeta)}{S(\zeta)}\mathrm{e}^{-p(\gamma_d(\zeta)(h+y)+\mathrm{i}\zeta x)/c_d}\mathrm{d}\zeta \\ &\quad +\frac{1}{2\pi}\int_{-\infty}^{\infty}\frac{2}{c_d}\frac{p\overline{F}(p)\zeta^2(2\zeta^2+k^2)}{S(\zeta)}\mathrm{e}^{-p(\gamma_d(\zeta)h+\gamma_s(\zeta)y+\mathrm{i}\zeta x)/c_d}\mathrm{d}\zeta, \qquad (2.2)\end{aligned}$$

where $\overline{F}(p)$ is the Laplace transform of $F(t)$ given by (1.2). The stress $\overline{\sigma}_{yy}$ in the solid is given by a similar Laplace transform

$$\begin{aligned}\overline{\sigma}_{yy}(x,y,p) &= \frac{1}{2\pi}\int_{-\infty}^{\infty}\frac{\mu}{2c_d^2}\frac{p^2\overline{F}(p)s(\zeta)(2\zeta^2+k^2)}{\gamma_d(\zeta)S(\zeta)}\mathrm{e}^{-p(\gamma_d(\zeta)(h+y)+\mathrm{i}\zeta x)/c_d}\mathrm{d}\zeta \\ &\quad -\frac{1}{2\pi}\int_{-\infty}^{\infty}\frac{4\mu}{c_d^2}\frac{p^2\overline{F}(p)\zeta^2(2\zeta^2+k^2)\gamma_s(\zeta)}{S(\zeta)}\mathrm{e}^{-p(\gamma_d(\zeta)h+\gamma_s(\zeta)y+\mathrm{i}\zeta x)/c_d}\mathrm{d}\zeta. \qquad (2.3)\end{aligned}$$

The plan is to discuss the response due to the normal displacement and identify asymptotic representations with particular attention to the non-geometric wavefront $S^\star$. The pressure in the fluid and stresses can then be similarly treated, but for brevity we exclude them here.

The Schölte function $S(\zeta)$ appears in both formulae, and is vital to the analysis; it is defined as $S(\zeta) = R(\zeta) + \varepsilon k^4 k'(\zeta^2+1)^{1/2}/(\zeta^2+k'^2)^{1/2}$. In this formula k and k' are defined to be the ratios c_d/c_s and c_d/c_o respectively. The Schölte function contains six branch points at $\pm\mathrm{i}, \pm\mathrm{i}k, \pm\mathrm{i}k'$, and either two or four zeros depending upon the precise choice of branch cuts. If $\varepsilon = 0$, that is, if the fluid is decoupled from the solid, the Schölte function is truncated to the function $R(\zeta)$. This is the standard Rayleigh function, $R(\zeta) = (2\zeta^2+k^2)^2 - 4\zeta^2(\zeta^2+1)^{1/2}(\zeta^2+k^2)^{1/2}$; this function has four branch points at $\pm\mathrm{i}, \pm\mathrm{i}k$, and two zeros at $\pm\mathrm{i}k_r$ where $k_r = c_d/c_r$ and c_r is the Rayleigh wavespeed ($k < k_r < k'$). The complement function $s(\zeta)$ defined as $s(\zeta) = r(\zeta) - \varepsilon k^4 k'(\zeta^2+1)^{1/2}/(\zeta^2+k'^2)^{1/2}$, where $r(\zeta) = (2\zeta^2+k^2)^2 + 4\zeta^2(\zeta^2+1)^{1/2}(\zeta^2+k^2)^{1/2}$, is also required.

The functions $\gamma_d(\zeta)$ that occur are defined as $\gamma_q(\zeta) = (\zeta^2+k_q^2)^{1/2}$, with $q = d,\ s,\ o$; $k_d = 1, k_s = k, k_o = k'$. Here the choice of branch cuts for the functions $\gamma_q(\zeta)$ in the complex ζ-plane is taken such that they run from $\pm\mathrm{i}k_q$ to $\pm\mathrm{i}\infty$ along the imaginary axis. With this choice of branch cuts the zeros of the Schölte function corresponding to leaky Rayleigh waves in the physical domain then occur on the lower Riemann sheet, and play no explicit role in the exact solution. Given the choice of branch cuts above, the Schölte function has only two zeros

at $\pm ik_{\text{sch}}$ where $k_{\text{sch}} = c_d/c_{\text{sch}}$ and c_{sch} is the Schölte wavespeed ($k_{\text{sch}} > k'$). This wavespeed is not related to the Rayleigh wavespeed, indeed for $\varepsilon \ll 1$ it is marginally less than the compressional wavespeed of the fluid in this limit. The following *migratory* behaviour of the zeros of $s(\zeta)$ from the imaginary axis, Roever *et al.* [18], is important. For low values of the Poisson's ratio both zeros of $s(\zeta)$ lie on the imaginary axis, the second zero lies close to the branch point at $-\text{i}$. As the Poisson's ratio is increased the zeros approach each other, intersect, and, typically at $0{\cdot}28 < \nu < 0{\cdot}3$, migrate from imaginary axis and form conjugate pairs. Typical results are that, for aluminium-water, $\pm ik_p = \mp 0{\cdot}15979 \pm \text{i}1{\cdot}01638$, and for sandstone-water, $\pm ik_p = \pm \text{i}0{\cdot}99912$, $\pm \text{i}0{\cdot}638995$.

The loading $F(t) = H(t)$, where $H(t)$ is the Heaviside step function, now reduces the integral equations to the form (1.3). This case is now considered in detail for the displacements for convenience, and is denoted by $u_y^H(x, y, t)$. To incorporate more general loadings, $F(t)$, we may utilise the following convolution theorem,

$$u_y(x, y, t) = \int_0^t F'(t-\tau) u_y^H(x, y, \tau) \mathrm{d}\tau \tag{2.4}$$

provided $F(0) = 0$.

The explicit solution is found using the Cagniard-de Hoop method, see for instance Miklowitz [4]. The displacement has been written above, in Equation (2.2), as the sum of two integrals, that is, in the form $\int g_1(\zeta)\mathrm{e}^{-pz_1(\zeta)}\mathrm{d}\zeta + \int g_2(\zeta)\mathrm{e}^{-pz_2(\zeta)}\mathrm{d}\zeta$ where the two functions z_1 and z_2 differ only by the function multiplying y. Two inversion contours are chosen so that $z_1(\zeta) = t$ and $z_2(\zeta) = t$, namely,

$$c_d t = (\zeta^{(P)^2} + 1)^{1/2}(h + y) + \text{i}\zeta^{(P)} x \quad \text{and} \tag{2.5}$$

$$c_d t = (\zeta^{(S)^2} + 1)^{1/2} h + (\zeta^{(S)^2} + k^2)^{1/2} y + \text{i}\zeta^{(S)} x, \tag{2.6}$$

These contours are used in turn in the integrals appearing in (2.2,2.3) to place each integral in the form of a Laplace transform. This amounts to a transformation of the Fourier integration path. As we ultimately require the inverse Laplace transform of this integral, our solution in real time is found immediately by inspection. The superscripts (P) and (S) relate to the compressional and shear disturbances respectively.

For the response in the solid the first Cagniard path (2.5), $\zeta^{(P)}(x, y, t)$, is found explicitly. The integration path is given by

$$\zeta^{(P)}(t) = -\text{i}\frac{c_d t}{r}\sin\theta + \left(\left(\frac{c_d t}{r}\right)^2 - 1\right)^{1/2}\cos\theta, \quad \text{for } t_{pp} \leqslant t < \infty, \tag{2.7}$$

where $t_{pp} = r/c_d$, $r^2 = x^2 + (h+y)^2$, and $\tan\theta = x/(h+y)$. This path is of less interest with regard to the asymptotic procedure. The situation for $y > 0$ is more complicated for the second Cagniard path (2.6), $\zeta^{(S)}(x, y, t)$, and the path is found numerically, or for either $h \ll x$ or $y \ll x$ via a perturbation analysis (the details are given in Section 2.2). From the formulation of a quartic algebraic equation, the full details are given in Williams [5], or via a Newton–Raphson algorithm, the Cagniard path $\zeta^{(S)}(t)$ is found numerically as the root of Equation (2.6) with positive real part. Using symmetry properties of the integrand it is sufficient to only consider the path in the fourth quadrant and this is given by taking the branch of $\zeta^{(S)}(t)$ with

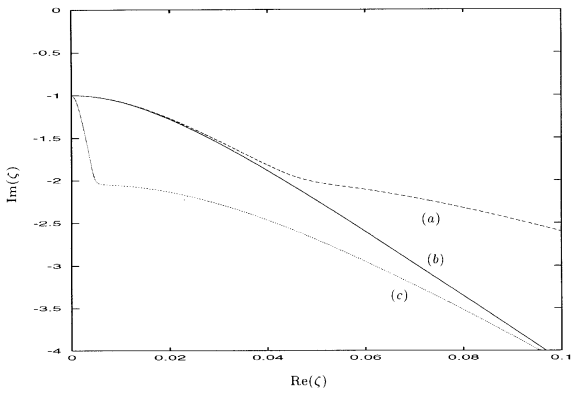

Figure 3. Three typical Cagniard paths for $\zeta^{(S)}(t)$. (*a*) $x/h = 40$, $y/h = 1$. (*b*) $x/h = 40$, $y/h = 0$. (*c*) $x/h = 400$, $y/h = 10$. Note the sharp bend in (*c*)

the positive square root. When $y = 0$ the integration path is already given explicitly by (2.7) where $r^2 = x^2 + h^2$ and $\tan\theta = x/h$.

In each case the Cagniard path, in the lower half plane, cuts the negative imaginary axis between 0 and -1. For particular choices of x/h and y/h the path departs from the axis very close to $-\mathrm{i}$; this can be seen in Figure 3 and in the next section in Figures 8 and 11. In Figure 3 a typical path for $h \ll x$ is shown and is labelled (*c*), this is distinctly different to the other two paths. In this limit the path approaches the branch point at $-\mathrm{i}$ and tightens around the branch cuts along the negative imaginary axis. In particular the path has a dramatic bend away from the axis near the saddle point that would exist at $-\mathrm{i}k\sin\theta$ in the case $h = 0$; in this case it is associated with the direct reflected shear arrival. Thus in the general case the situation is similar to that when $y = 0$, except that we usually have to find both the path and t_{ps} $(= t_{\text{critical}})$ numerically.

The exact solution for the vertical displacement in $y > 0$, written as a function of t, is simply

$$u_y^H(x, y, t) = -\frac{1}{2\pi c_d} H(t - t_{pp}) \mathfrak{Re}\left(\frac{s(\zeta^{(P)})}{S(\zeta^{(P)})}\frac{\mathrm{d}\zeta^{(P)}(t)}{\mathrm{d}t}\right) + \frac{2}{\pi c_d} H(t - t_{ps}) \mathfrak{Re}\left(\frac{\zeta^{(S)^2}(2\zeta^{(S)^2} + k^2)}{S(\zeta^{(S)})}\frac{\mathrm{d}\zeta^{(S)}(t)}{\mathrm{d}t}\right), \tag{2.8}$$

where t_{pp} and t_{ps} $(= r/c_d$ when $y = 0)$ correspond to the arrival of the PP and PS waves respectively and $\zeta^{(P)}(t)$, $\zeta^{(S)}(t)$ are the paths described above.

The wavefront arrivals are shown for $\pi c_d u_y^H(x, y, t)$ versus t in Figure 4 for typical values of x, y, and h. The ratios x/h and y/h determine the shape of the response; we have avoided rescaling each figure by h for convenience. The material parameters, Briggs [19], are taken to be typical of sandstone-water configuration; c_d and c_s are 2920 m/s and 1840 m/s respectively, and c_o is 1480 m/s, the solid and fluid densities are 2440 kg/m^3 and 1000 kg/m^3 respectively. Also shown on these figures are asymptotic representations for the dominant responses; the expressions are not given here, but are found following Williams [5]. The lines denoted by t_{pp}, t_{ps}, t_l, and t_{sch} are the arrival times associated with the PP, PS, leaky Rayleigh, and Schölte waves respectively. The non-geometric $S^\star$ arrival is denoted by an arrival time $t_{s^\star}$.

In Figure 4 the compressional wave in the solid arrives first at $t = t_{pp}$, and this is shortly followed by the shear wave at $t = t_{ps}$. The shape of these arrivals is brought about in each case by the branch points or poles that lie close to the path. The Schölte wave generates a distinctive response that dominates the leaky wave that precedes it; nevertheless the leaky wave has a definite shape that here persists, away from a light fluid loading limit. The piece of the Cagniard path that gives the contribution leading to the compressional wavefront arrival is often close to a zero of the Schölte complement function $s(\zeta)$. The importance of the zeros of this function are that the sign of the singularity associated with this response may change, this phenomenon is not illustrated.

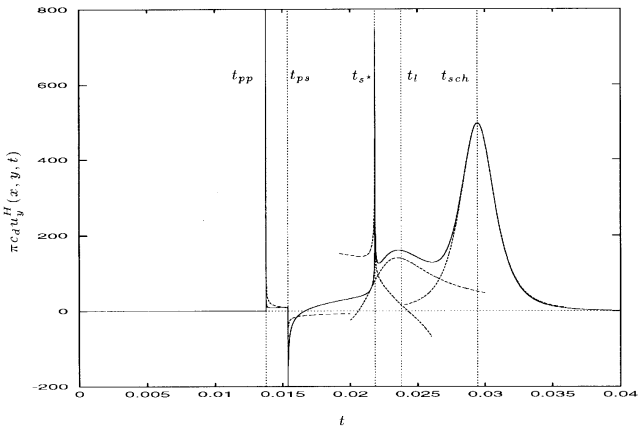

Figure 4. A plot of $\pi c_d u_y^H(x, y, t)$ versus t for material parameters typical of sandstone/water; $x = 40$, $y = 4$, $h = 0{\cdot}01$. The asymptotic results are the dashed lines.

An additional shear response, that is $S^\star$, is visible for small h, see the discussion of Section 2.2. This response is shown in detail in Figure 5, together with an asymptotic representation.

2.2. THE SOURCE CLOSE TO THE INTERFACE

In this section we investigate directly the signals associated with non-geometric arrivals. These arrivals only give large responses when the source is close to the interface, that is, when h is small. As h increases their effect is diminished. We have already observed that in the limit $h/x \to 0$ the Cagniard path is distinctly different to the typical path, see Figure 3(a, b) and (c). This motivates us to examine the Cagniard path, and we crucially identify the $S^\star$ arrival with the sharp bend in the path in the limit $h/x \to 0$; in Figure 3(c). The physical significance of the bend in the path has also been observed by Hron and Mikhailenko [6].

In the limiting case $h = 0$, corresponding to the source on the interface, the path, $\zeta^{(S)}(t)$, consists of a piece running directly along the branch cuts from $\zeta^{(S)} = -\mathrm{i}$ to $\zeta^{(S)} = -\mathrm{i}k \sin\theta$ together with a hyperbolic path; in these formulae, $x = r \sin\theta$, $y = r \cos\theta$. The point $\zeta^{(S)} = -\mathrm{i}k \sin\theta$, where the path leaves the imaginary axis, is the saddle point in a steepest descents analysis and gives wavefronts travelling with wavespeed c_s due to a shear wave, S, generated within the solid. This is shown in Figure 2. When $h \ll x$ the path runs from $-\mathrm{i}\zeta_{ps}$ very close to the branch cuts before turning away dramatically at approximately $\zeta^{(S)} \sim -\mathrm{i}k \sin\theta$. This point generates the distinctive response $S^\star$ in the solid when $t \sim r/c_s = t_{s^\star}$. The Cagniard-de Hoop technique identifies this response; it is useful to analyse the structure of the response by constructing an asymptotic representation.

As an alternative to finding the Cagniard path numerically we find a useful asymptotic representation for the path, when h is small, by perturbing away from the $h = 0$ path. That is, we consider the path

$$\zeta_p^{(S)}(t) = \zeta_{h0}(t) + h\zeta_{h1}(t) \tag{2.9}$$

where $\zeta_{h0}(t)$ is simply the solution to $c_d t = (\zeta_{h0}^2 + k^2)^{1/2} y + \mathrm{i}\zeta_{h0} x$. This is found explicitly as

$$\zeta_{h0}(t) = \begin{cases} -\mathrm{i}\dfrac{c_d t}{r}\sin\theta + \mathrm{i}k\left(1 - \left(\dfrac{c_s t}{r}\right)^2\right)^{1/2}\cos\theta \quad \text{when } t_{h0} \leqslant t < \dfrac{r}{c_s}, \\ -\mathrm{i}\dfrac{c_d t}{r}\sin\theta + k\left(\left(\dfrac{c_s t}{r}\right)^2 - 1\right)^{1/2}\cos\theta \quad \text{when } \dfrac{r}{c_s} \leqslant t < \infty, \end{cases} \tag{2.10}$$

where $t_{h0} = (x + y(k^2 - 1)^{1/2})/c_d$. In this formula $r^2 = x^2 + y^2$ and $\tan\theta = x/y$. Utilising the path (2.9) in the transcendental Equation (2.6), the perturbation term $\zeta_{h1}(t)$ is found to be

$$\zeta_{h1}(t) = -\zeta_{h0}(\zeta_{h0}^2 + 1)^{1/2}\left(c_d t - \frac{k^2 y}{(\zeta_{h0}^2 + k^2)^{1/2}}\right)^{-1}, \tag{2.11}$$

but crucially the denominator in expression (2.11) is zero at $\mathrm{d}t(\zeta_{h0})/\mathrm{d}\zeta_{h0} = 0$ and this occurs when $\zeta_{h0} = -ik\sin\theta$ at arrival time $t_{s\star}$. It follows that the representation (2.9) is only valid outside some close interval of $t_{s\star}$. It is an unfortunate consequence of perturbing away from the explicit zero path that the perturbed path we find is invalid for $|t - t_{s\star}| < t_\varepsilon = O(h/c_d)$. This non-uniformity is because the part of the zero path that sharply departs from the imaginary axis leads to a large change in (2.11). The exact path found numerically contains a smoothing term of order $\mathrm{i}h$.

In addition, we may construct a similar expression for the derivative of the path via a direct differentiation of equation (2.9) or expanding an expression for the path in the derivative of the path (2.6); this is a vital part of the explicit solution

$$\frac{\mathrm{d}\zeta_p^{(S)}}{\mathrm{d}t} \sim \frac{\mathrm{d}\zeta_{h0}}{\mathrm{d}t} - h\frac{\left(c_d t - k^2 y(\zeta_{h0}^2 + k^2 + \zeta_{h0}^2 + 1)(\zeta_{h0}^2 + k^2)^{-3/2}\right)}{c_d^2(\zeta_{h0}^2 + 1)^{1/2}}\left(\frac{\mathrm{d}\zeta_{h0}}{\mathrm{d}t}\right)^3, \tag{2.12}$$

where

$$\frac{\mathrm{d}\zeta_{h0}}{\mathrm{d}t} = c_d\zeta_{h0}\left(c_d t - \frac{k^2 y}{(\zeta_{h0}^2 + k^2)^{1/2}}\right)^{-1}. \tag{2.13}$$

There is some interest in near surface responses, that is, when the receiver depth y is also small. We construct an asymptotic representation for the Cagniard path when y is small by following the approach described above, and now perturbing away from the explicit $y = 0$ path. Once again, we consider $\zeta_p^{(S)}(t) = \zeta_{y0}(t) + y\zeta_{y1}(t)$ where the perturbation $\zeta_{y1}(t)$ is

$$\zeta_{y1}(t) = -\zeta_{y0}(\zeta_{y0}^2 + k^2)^{1/2}\left(c_d t - \frac{y}{(\zeta_{y0}^2 + 1)^{1/2}}\right)^{-1}. \tag{2.14}$$

The smooth behaviour of the $y = 0$ path, see Figure 3(b), avoids any difficulty close to $t_{s^\star}$. In Figure 6 we show an approximation to the $S^\star$ arrival in the restricted case $h \ll y \ll x$.

From the discussion above we see that when $h \ll x$ the response associated with the $S^\star$ wave at $t_{s^\star} \sim r/c_s$ begins to emerge. The displacement in the neighbourhood of $t_{s^\star}$ is then given as

$$u_y^H(x, y, t) \sim -\frac{1}{2\pi c_d}\mathfrak{Re}\left(\frac{s(\zeta^{(P)})}{S(\zeta^{(P)})}\frac{\mathrm{d}\zeta^{(P)}(t)}{\mathrm{d}t}\right) + \frac{2}{\pi c_d}\mathfrak{Re}\left(\frac{\zeta^2(2\zeta^2 + k^2)}{S(\zeta)}\Big|_{\zeta=-\mathrm{i}k\sin\theta}\frac{\mathrm{d}\zeta_p^{(S)}(t)}{\mathrm{d}t}\right), \tag{2.15}$$

where $\zeta^{(P)}(t)$ and $\zeta_p^{(S)}(t)$ are given by Equations (2.7) and (2.9, 2.10, 2.11) respectively.

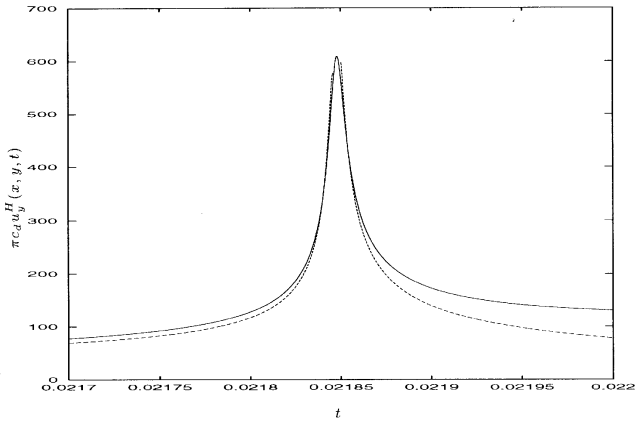

Figure 5. The exact and asymptotic expressions for $\pi c_d u_y^H(x, y, t)$ versus t in the region near $t_{s^\star}$ in Figure 4; $x = 40$, $y = 4$, $h = 0{\cdot}01$. Material parameters are sandstone/water.

In Figure 5 we compare the exact and asymptotic solutions for the normal displacement. The basic features of the $S^\star$ arrival have been preserved. The position and shape of the response is well predicted before and after $t_{s^\star}$. The asymptotic representation for the displacement when we are in the close neighbourhood of the interface so that $h \ll y \ll x$ is shown in Figure 6. Now the shape of the response is well matched almost everywhere. There can, however, be a reasonable difference in the size and position of the exact and approximate responses. This is principally due to the interference of nearby wavefronts.

As we increase y the wavefronts move closer, particularly in this rock-water case, nonetheless the asymptotics are still accurate. The leaky Rayleigh response may be masked and interfere with the non-geometric shear arrival that dominates.

The arrival time of the PS wave, t_{ps}, is the first arrival and is typically found numerically. Often it is a useful characteristic and we determine its approximate form, when $h \ll x$, be seeking a solution to $\mathrm{d}t(\zeta_{ps})/\mathrm{d}\zeta_{ps} = 0$ in the form $\zeta_{ps} = -\mathrm{i} + \mathrm{i}\zeta_{ps}^{\varepsilon}$ where $\zeta_{ps}^{\varepsilon} \ll 1$. Thus we find that

$$c_d t_{ps} \sim x + y(k^2 - 1)^{1/2} + h^2\left(x - \frac{y}{(k^2 - 1)^{1/2}}\right)^{-1}. \tag{2.16}$$

For $h/x \ll 1$ this provides the small curvature correction from the straight head wave wavefront found when $h = 0$. The head waves are confined to the region defined by $c_s t \leqslant r \leqslant$

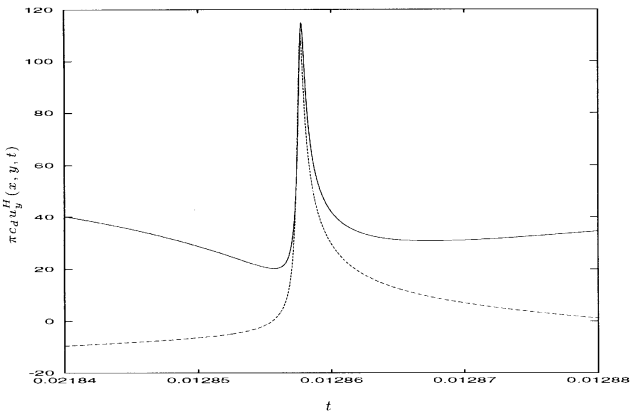

Figure 6. The exact and asymptotic expressions for $\pi c_d u_y^H(x, y, t)$ versus t in the region near $t_{s^\star}$ in the case $h \ll y \ll x$; $x = 40$, $y = 0{\cdot}1$, $h = 0{\cdot}0008$. Material parameters are aluminium/water.

$c_d t(\sin\theta + (k^2 - 1)^{1/2}\cos\theta)^{-1}$ and $\sin^{-1} c_s/c_d \leqslant \theta \leqslant \pi/2$. In these formulae $x = r\cos\theta$, $y = r\sin\theta$.

3. A compressional source beneath a thin high velocity layer

The previous section described the tunnelling effects in dissimilar material half spaces due to either material mismatch, or wave coupling at the interface. Another example of tunnelling occurs when a thin, high velocity layer lies embedded within a slow surrounding material. For illustrative purposes we first consider a source above a fluid layer, see for instance Mellman and Helmberger [7], Drijkoningen and Chapman [8], and use generalised ray theory to identify the explicit solution for the wavefronts transmitted through the layer. We then move on to treat the more relevant elastic problem. The tunnelling response is the perturbation caused to the cylindrical wavefront that would, in the absence of the layer, be seen. Instead of a sharp, singular, wavefront some smoothing that is dependent upon the layer thickness occurs, and we aim to find this dependence.

It turns out that under certain conditions on the source depth and layer thickness only one generalised ray contributes to the tunnelling response. We may then analyse this path in a similar manner to the previous section. This avoids having to consider the complete generalised ray expansion and we are able to neatly pick out the non-geometric response. Importantly, we are able to identify these conditions and further make a prediction when a second ray becomes important.

When we proceed to treat the more complicated elastic analogue, that is, a compressional source and an elastic layer between two elastic half spaces, and look at the transmitted compressional wavefront, a similar simplification can be employed thus avoiding rather complicated sums of rays.

3.1. A FLUID LAYER

As a brief illustrative example of the generalised theory and our perturbation scheme on the leading generalised ray we first treat the equivalent fluid problem, that is, the shear ray path is absent from the schematic in Figure 7. The fluid is again assumed to be compressible, and

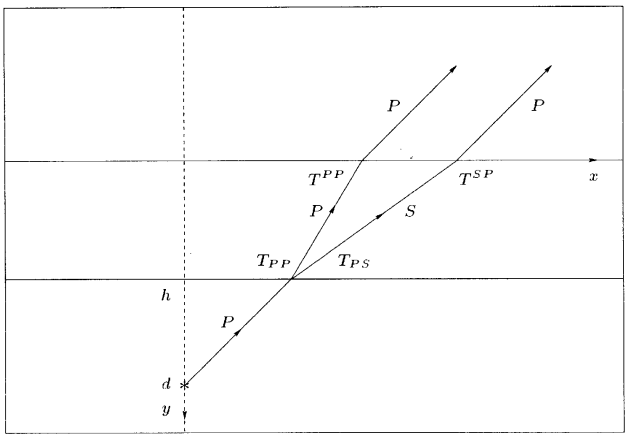

Figure 7. The geometry of a typical configuration considered in the text. The layer occupies $0 < y < h$ and the semi-infinite space $y > h$ contains a source at depth d. The paths of the generalised rays are shown to illustrate the tunnelling response; the letters P and S denote the wave type and the transmission coefficients are included at the interfaces.

has density ρ_1 and wavespeed c_1, apart from the layer in $0 < y < h$, that has density ρ_2 and wavespeed c_2 ($c_2 > c_1$). The governing equations follow those outlined in Section 2 and the equivalent source equation is given following Equation (2.1).

We employ the method of generalised rays, see for instance Pao and Gajewski [20], to derive the solution. In essence the multiply reflected and refracted waves in the solution are represented by a series of ray integrals. Each integral is then evaluated exactly using the Cagniard-de Hoop method and the exact solution is then found up to the arrival of the next ray.

In the fluid for $y < 0$ the Laplace transform of the normal displacement is

$$\overline{u}_y(x, y, p) = \frac{1}{2\pi}\int_{-\infty}^{\infty} \frac{1}{2c_2} p\overline{F}(p) T_{PP}(\zeta) T^{PP}(\zeta) \times \sum_{m=0}^{\infty} \left(R_{PP}(\zeta) R^{PP}(\zeta)\right)^m \mathrm{e}^{-pZ_m(\zeta)} \mathrm{d}\zeta \tag{3.1}$$

where $Z_m(\zeta) = (\gamma_1(\zeta)(d-h-y)+(2m+1)\gamma_2(\zeta)h+\mathrm{i}\zeta x)/c_2$. The reflection and transmission coefficients, which are usually given as functions of angle of incidence, Ewing *et al.* [21], are expressed in terms of ζ in Appendix A. The ratios of the transmitted and reflected waves to the incident waves are denoted by the letters T and R respectively. We have introduced the rescaling $\xi = p\zeta/c_2$ for convenience. In this formula ρ is defined to be the ratio ρ_2/ρ_1 and $\overline{F}(p)$ is the Laplace transform of $F(t)$ given by (1.2). The functions $\gamma_1(\zeta)$, $\gamma_2(\zeta)$ that appear are defined as $(\zeta^2 + k^2)^{1/2}$, $(k = c_2/c_1)$ and $(\zeta^2 + 1)^{1/2}$ respectively.

To calculate the exact solution utilising the Cagniard-de Hoop method, a Cagniard path for each of the generalised rays is determined by setting $Z_m(\zeta) = t$, that is

$$c_2 t = \gamma_1(\zeta_m)(d - y - h) + (2m + 1)\gamma_2(\zeta_m)h + \mathrm{i}\zeta_m x \tag{3.2}$$

so that $\zeta_m(t)$ is the root of this equation typically found numerically. In Figure 8 typical Cagniard paths are shown. The path departs from the negative imaginary axis at $-\mathrm{i}\zeta_m$, between

0 and $-\mathrm{i}$ at time t_m. Using (3.2) t_m, the arrival time of the direct geometrical wave, is determined by the condition $\mathrm{d}t(\zeta_m)/\mathrm{d}\zeta_m = 0$. This corresponds to a combined contribution of a geometric and a head wave type arrival. The other, and more important, feature of the path is the bend; this is the part of the path that we are interested in since it gives us the tunnelling ray.

First consider the behaviour of the first path ($m = 0$). This path runs close to the imaginary axis before sharply bending away near $-\mathrm{i}k\sin\theta$ at $t \sim r/c_1 = t_{p^\star}$ ($x = r\sin\theta$, $d - y = r\sin\theta$). This sharp bend has been observed by Drijkoningen [9]. The change in the shape of the path typically becomes less pronounced as h is increased, and in particular, the bend is less prominent. When $h = 0$ the Cagniard paths are all equivalent. Otherwise the paths are separate, however when h is *very* small, several paths now have a significant bend. The bend in each of these paths now contribute to the tunnelling signal, and our analysis then requires modification.

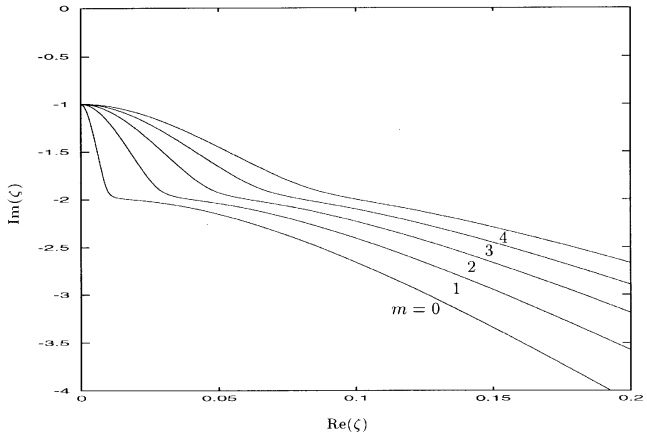

Figure 8. Typical Cagniard paths $\zeta_m(t)$, for values of $m = 0, 4$ as labelled.

A useful asymptotic representation for the path when h is small is found following the scheme described in Section 2.2, that is, by perturbing away from the $h = 0$ path. We consider $\zeta_{m,p}(t) = \zeta_{h0}(t) + h\zeta_{m,h1}(t)$ where $\zeta_{h0}(t)$ is for all values of m simply the solution to $c_2 t = (\zeta_{h0}^2 + k^2)^{1/2}(d - y) + \mathrm{i}\zeta_{h0}x$. Now the perturbation $\zeta_{m,h1}(t)$ is

$$\zeta_{m,h1}(t) = \zeta_{h0}((\zeta_{h0}^2 + k^2)^{1/2} - (2m+1)(\zeta_{h0}^2 + 1)^{1/2})\left(c_2 t - \frac{k^2(d-y)}{(\zeta_{h0}^2 + k^2)^{1/2}}\right)^{-1}. \tag{3.3}$$

This approximation to the path is identical to the path found numerically outside some small interval of $t_{p^\star}$ as discussed in Section 2.2. Indeed, Equation (3.3) performs well for greater values of h, and is not exclusive to the first path ($m = 0$).

In addition we determine an approximate form for t_m be seeking a solution to (3.2) of the form $\zeta_m = -\mathrm{i} + \mathrm{i}\zeta_m^{\varepsilon}$ where $\zeta_m^{\varepsilon} \ll 1$;

$$c_2 t_m = x + (d - y - h)(k^2 - 1)^{1/2} + (2m+1)^2 h^2 \left(x - \frac{(d-y-h)}{(k^2-1)^{1/2}}\right)^{-1}. \tag{3.4}$$

The following numerical results are calculated for the loading $F(t) = H(t)$. Other loadings may be incorporated as described in Section 2. In Figure 9 the exact response $\pi c_2 u_y^H$

$(x, y, t)/2\rho$ is plotted against t for $c_2/c_1 = 2$ and $\rho_2/\rho_1 = 1.4$, together with an asymptotic representation for the tunnelling wave and the first solution ($m = 0$). The total (added) solution is described by the summed response in the figures, and is taken for values of m up to $m = 24$. There are a succession of square root singularities associated with the geometrical wave; the singularities appear very close together in the figures shown. In the added response the different rays interfere. The head wave arrivals are altered when we include many multiples. The shape of the first response has almost completely disappeared, see for instance Mellman and Helmberger [7], where similar behaviour is discussed. The waves that have been multiply reflected in the layer interfere with the size of the tunnelling wave and can cause a reasonable offset, however, the shape of the arrival is not very different from the response due to the tunnelling only once. This direct tunnelling signal is completely captured by the first path in this case. We identify a wavefront expansion for the tunnelling signal in a similar manner to Equation (2.15) in Section 2.2.

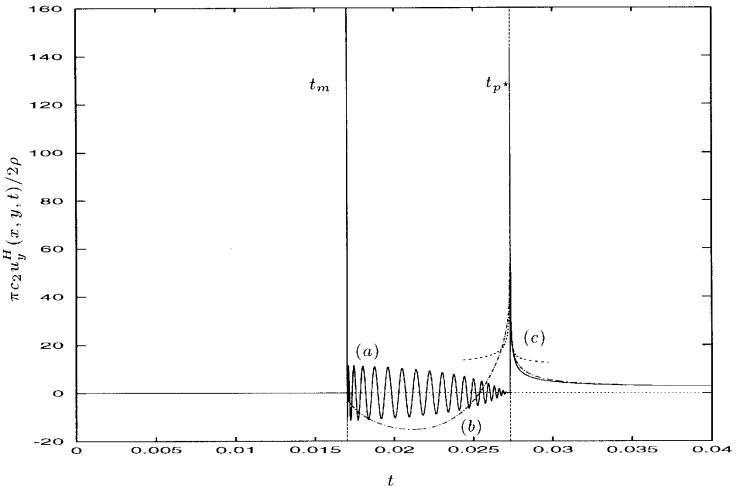

Figure 9. A plot of $\pi c_2 u_y^H(x, y, t)/2\rho$ versus t in $y < 0$; $x = 40$, $y = -4$, $h = 0{\cdot}004$, $d = 2$. (*a*) Summed response up to $m = 24$. (*b*) Exact response $m = 0$. (*c*) Approximation $m = 0$.

The displacement in the neighbourhood of $t_{p^\star}$ is given as

$$u_y^H(x, y, t) = \frac{2\rho}{\pi c_2} \Re\mathfrak{e} \left(\frac{\gamma_1(\zeta)\gamma_2(\zeta)}{(\gamma_2(\zeta) + \rho\gamma_2(\zeta))^2} \Big|_{\zeta = -ik\sin\theta} \frac{\mathrm{d}\zeta_{0,p}(t)}{\mathrm{d}t} \right). \tag{3.5}$$

The last term can be written in a more explicit form using (3.3). In Figure 10 we compare the exact response with the approximate response. The basic features of the tunnelling signal have been preserved, and both the shape and size of the leading solution are well matched. The multiply reflected arrivals can cause a considerable size difference to exist between the exact and approximate solutions. Nonetheless the direct tunnelling wave, a key feature in the wave field, is itself well predicted. In other cases when h becomes very small, we need a second generalised ray to fully capture the wavefront that has tunnelled through the layer, and then expect to represent this wavefront by a sum of expressions like (3.5), involving $\zeta_{m,p}$ for $m = 0, 1, \ldots$

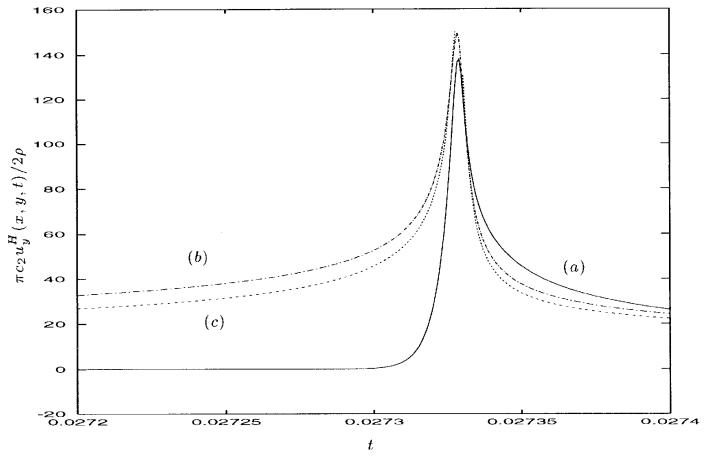

Figure 10. The exact and asymptotic expressions for $\pi c_2 u_y^H(x, y, t)/2\rho$ versus t in the region near $t_{p^\star}$ in Figure 9. (*a*) Summed response up to $m = 24$. (*b*) Exact response $m = 0$. (*c*) Approximation $m = 0$.

3.2. AN ELASTIC LAYER

We now proceed to treat the more relevant elastic layer problem. As shown in Section 3.1 the generalised ray theory yields the exact solution to the model problem up to the arrival of the next ray. Moreover, this approach directly constructs the ray integrals, thus avoiding any laborious matrix determination, see for instance the discussion in Kennett [22]. This enables us to pick out the main features associated with the leading arrivals directly with a minimum of work.

Now consider a line compressional source at $y = d$ beneath an elastic layer, thickness h; the geometry is shown in Figure 7. The elastic material has density ρ_1 and compressional and shear wavespeeds c_{d1} and c_{s1}, apart from the layer in $0 < y < h$, that has density ρ_2 and wavespeeds c_{d2}, c_{s2}; we assume that $c_{d2} > c_{d1} > c_{s2} > c_{s1}$. The governing equations follow those outlined in Section 2 and the equivalent source equation is given following Equation (2.1).

We now proceed to derive the solution. At each of the interfaces $y = 0$ and $y = h$ we have to satisfy four continuity conditions: the continuity of the stresses σ_{yy} and σ_{xy}, and the continuity of the displacements u_x and u_y. Instead of determining the coefficients from a system of eight simultaneous equations and then constructing the ray integrals we prefer to employ the method of generalised rays, see for instance Pao and Gajewski [20] and the discussion of Section 3.1.

We have already observed, when treating the fluid layer, that the shape of the wavefronts in the summed solution closely resembles the response given only by the leading generalised ray. The equivalent physical approximation leads us to consider only the transmitted waves in the layer; the multiply reflected and refracted waves are omitted. The compressional part of the transmitted wave in the layer is obtained by superimposing all transmitted P waves, together with the source function

$$\overline{u}_y(x, y, p) = -\frac{1}{2\pi}\int_{-\infty}^{\infty} \frac{1}{2c_{d2}} p\overline{F}(p) \times (T_{PP}T^{PP}\mathrm{e}^{p\gamma_{s2}h/c_{d2}} + T_{PS}T^{SP}\mathrm{e}^{p\gamma_{d2}h/c_{d2}})\mathrm{e}^{-p((\gamma_{d2}+\gamma_{s2})h+\gamma_{d1}(d-h-y)+\mathrm{i}\zeta x)/c_{d2}}\mathrm{d}\zeta. \quad (3.6)$$

The reflection and transmission coefficients in this formula are expressed in terms of ζ in Appendix A together with a brief description of the notation. In addition the functions γ_{d2}, γ_{s2}, γ_{d1}, and γ_{s1} that appear are defined. We have introduced the following wavespeed ratios $k_{d2} = 1$, $k_{s2} = c_{d2}/c_{s2}$, $k_{d1} = c_{d2}/c_{d1}$, and $k_{s1} = c_{d2}/c_{s1}$.

A generalised ray path has been constructed to connect the source and receiver for each transmitted waves, see Figure 7. The path describes the vertical distance travelled by each mode of waves in each layer, the total horizontal distance, and the direction of propagation. The two Cagniard paths in this case are now found by identifying the ray paths with t, that is, setting

$$c_{d2}t = \gamma_{d1}(\zeta_1)(d - h - y) + \gamma_{d2}(\zeta_1)h + \mathrm{i}\zeta_1 x, \tag{3.7}$$

$$c_{d2}t = \gamma_{d1}(\zeta_2)(d - h - y) + \gamma_{s2}(\zeta_2)h + \mathrm{i}\zeta_2 x. \tag{3.8}$$

The subscripts 1 and 2 on ζ have been introduced to describe the first and second paths. Note that when $h = 0$ the two paths are equivalent. Both Cagniard paths $\zeta_1(t)$ and $\zeta_2(t)$ are again found numerically and are shown in Figure 11. As we have already observed the paths have two main features. First the path leaves the negative axis. For the first path this occurs at $-\mathrm{i}\zeta_p$ ($0 < \zeta_p < 1$), the second path has a piece lying along the negative axis from $-\mathrm{i}$ to $-\mathrm{i}\zeta_s$ ($1 < \zeta_s < k_{d1}$). In both cases the intersection occurs at $\mathrm{d}t(\zeta)/\mathrm{d}\zeta = 0$ and this corresponds to the direct geometrical arrival. The branch point at $-\mathrm{i}$ causes a head wave in the second path. The second and more interesting feature is the sharp bend in the path, that we have previously identified with the non-geometric and tunnelling signals; the two paths bend away at approximately $-\mathrm{i}k_{d1}\sin\theta$ and $-\mathrm{i}k_{s2}\sin\theta$.

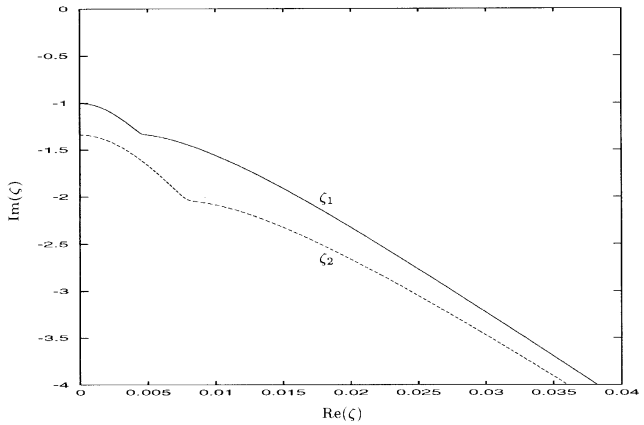

Figure 11. The Cagniard paths $\zeta_1(t)$ and $\zeta_2(t)$ for $x/h = 200$ and $(d - y)/h = 2$.

The exact solution for the direct transmitted compressional part of the normal displacement in $y < 0$ may now be extracted utilising the Cagniard method; it is not included here. Moreover, we may employ our perturbation scheme to find a further asymptotic representation for the ζ_1 path when h is small. Thus $\zeta_{1,p}(t) = \zeta_{h0}(t) + h\zeta_{1,h1}(t)$, where $\zeta_{h0}(t)$ is again the explicit zero path and the perturbation $\zeta_{1,h1}(t)$ is

$$\zeta_{1,h1}(t) = \zeta_{h0}\left((\zeta_{h0}^2 + k_{d1}^2)^{1/2} - (\zeta_{h0}^2 + 1)^{1/2}\right)\left(c_{d2}t - \frac{k_{d1}^2(d - y)}{(\zeta_{h0}^2 + k_{d1}^2)^{1/2}}\right)^{-1}, \tag{3.9}$$

The ζ_2 path is well predicted by the zero path since t_{sp} is close to $t_{p^\star} = r/c_{d1}$, and leaves the imaginary axis at $\zeta_{sp} - \delta$ for some $\delta \ll 1$; the second bend in the path occurs near $t = r/c_{s2}$.

In Figure 12 the leading compressional response $2\pi c_{d2} u_y^H$ is plotted against t. To demonstrate the tunnelling signal, the material parameters of aluminium and copper, typical of a fast and slow material are utilised. The density of copper is 8933 kg/m^3 with compressional and shear wavespeeds 4759 m/s and 2325 m/s respectively, and aluminium density is 2700 kg/m^3 with compressional and shear wavespeeds 6374 m/s and 3111 m/s respectively. The material parameters are taken from Briggs [19] and Bradfield [23].

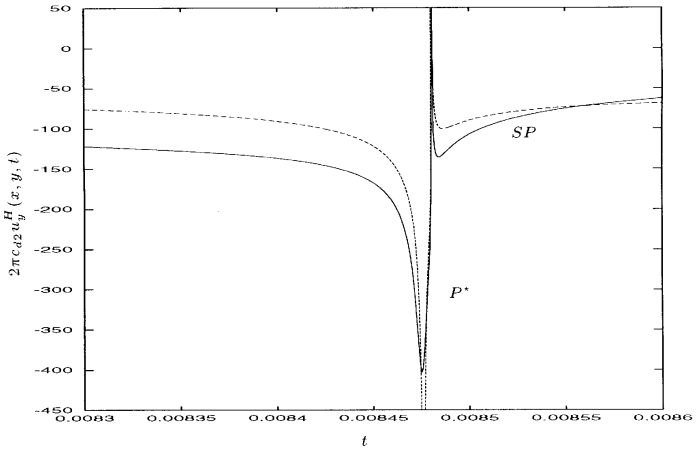

Figure 12. The exact and asymptotic expressions for $2\pi c_{d2} u_y^H(x, y, t)$ versus t in the region near $t_{p^\star} = r/c_{d1}$ and t_{sp}. (*a*) Tunnelling wave. (*b*) Direct compressional wave sp.

In the figure the geometric wave, SP generated by the shear wave in the layer arrives at t_{sp}. Immediately prior to this arrival is the sharp non-geometrical wavefront that we identify as $P^\star$, the cylindrical wave in the case $h = 0$. The asymptotic expression performs well and correctly matches the position and shape of the tunnelling signal. This is particularly useful, since other asymptotic approaches are awkward to evaluate, particularly close to a direct geometric arrival.

4. Conclusion

Tunnelling rays in dissimilar and layered materials are ideally suited to analysis via the Cagniard-de Hoop method, and we examine two canonical problems. In each case an asymptotic representation of the Cagniard path is found, thus explicit and highly accurate solutions when $h/x \to 0$ are obtained. This perturbation approach of generating Cagniard paths bypasses any numerical work, and should be useful in the asymptotic study of a range of related problems.

In each case we approximate the exact response and obtain simple expressions for the tunnelling signal. A particularly useful aspect is that the approximation to the tunnelling signal does not rely on an explicit expression for the contour.

In the example of a thin high velocity layer we have obtained the tunnelling ray using generalised ray theory.

The results presented here will be valuable in formulating more realistic fluid-solid interaction problems. The treatment may be routinely extended to examine the equivalent three

dimensional problems as well as to dipping structures, see for instance Hong and Helmberger [24], Pao *et al.* [25]. Since one is freed from the numerical calculation of many Cagniard paths, one can consider more complicated scenarios and further extensions may be to examine fluid-layered elastic, anisotropic media and model problems involving cracks beneath interfaces and multiple reflections.

Appendix A. Reflection and transmission coefficients

The relevant reflection and transmission coefficients required in Section 3.1 are

$$\begin{aligned} T_{PP}(\zeta) &= \frac{2\gamma_1(\zeta)}{(\gamma_2(\zeta)+\rho\gamma_1(\zeta))}, \qquad T^{PP}(\zeta) = \frac{2\rho\gamma_2(\zeta)}{(\gamma_2(\zeta)+\rho\gamma_1(\zeta))}, \\ R_{PP}(\zeta) &= R^{PP}(\zeta) = \frac{\gamma_2(\zeta)-\rho\gamma_1(\zeta)}{\gamma_2(\zeta)+\rho\gamma_1(\zeta)}. \end{aligned} \tag{A 1}$$

The subscripts 1 and 2 are used to denote the fluids in $y < 0$, $y > h$, and in $0 < y < h$. In these formulae $\rho = \rho_2/\rho_1$ and the functions γ_1 and γ_2 are defined as $(\zeta^2 + k^2)^{1/2}$ $(k = c_2/c_1)$ and $(\zeta^2 + 1)^{1/2}$.

The relevant reflection and transmission coefficients required in Section 3.2 are

$$\begin{aligned} T_{PP} &= \gamma_{d1}(\xi^2 - \gamma_{s1}^2)\left(\mu(\gamma_{s1}\zeta^2 + \gamma_{s1}\gamma_{s2}^2 - 2\gamma_{s2}\zeta^2) + (\gamma_{s2}\zeta^2 + \gamma_{s2}\gamma_{s1}^2 - 2\gamma_{s1}\zeta^2)\right)\Delta, \\ T^{PP} &= \mu\gamma_{d2}(\xi^2 - \gamma_{s2}^2)\left(\mu(\gamma_{s1}\zeta^2 + \gamma_{s1}\gamma_{s2}^2 - 2\gamma_{s2}\zeta^2) + (\gamma_{s2}\zeta^2 + \gamma_{s2}\gamma_{s1}^2 - 2\gamma_{s1}\zeta^2)\right)\Delta, \\ T_{PS} &= \mathrm{i}\zeta\gamma_{d1}(\xi^2 - \gamma_s^2)\left(-\mu(\zeta^2 + \gamma_{s2}^2 - 2\gamma_{s1}\gamma_{d2}) + (\zeta^2 + \gamma_{s1}^2 - 2\gamma_{s1}\gamma_{d2})\right)\Delta, \\ T^{SP} &= \mathrm{i}\mu\zeta\gamma_{s2}(\xi^2 - \gamma_s^2)\left(-\mu(\zeta^2 + \gamma_{s2}^2 - 2\gamma_{s1}\gamma_{d2}) + (\zeta^2 + \gamma_{s1}^2 - 2\gamma_{s1}\gamma_{d2})\right)\Delta, \end{aligned} \tag{A 2}$$

where

$$\begin{aligned} \Delta &= 2\,(\delta_1 + \delta_2 + \delta_3 + \delta_4)^{-1}, \\ \delta_1 &= (\zeta^2 - \gamma_{d2}\gamma_{s2})R_1(\zeta), \qquad \delta_2 = \mu^2(\zeta^2 - \gamma_{d1}\gamma_{s1})R_2(\zeta), \\ \delta_3 &= -2\mu\zeta^2(\zeta^2 + \gamma_{s2}^2 - 2\gamma_{d2}\gamma_{s2})(\zeta^2 + \gamma_{s1}^2 - 2\gamma_{s1}\gamma_{d1}), \\ \delta_4 &= -\mu(\gamma_{d1}\gamma_{s2} + \gamma_{d2}\gamma_{s1})(\zeta^2 - \gamma_{s1}^2)(\zeta^2 - \gamma_{s2}^2). \end{aligned} \tag{A 3}$$

The subscripts 2 and 1 are used to denote the elastic material in $0 < y < h$ and in $y < 0$, $y > h$ respectively. In these formulae $\mu = \mu_2/\mu_1$ and the functions γ_{d2}, γ_{s2}, γ_{d1}, and γ_{s1} are defined as $\gamma_{q2} = (\zeta^2 + k_{q2}^2)^{1/2}$, with $q = d, s$, and $\gamma_{q1} = (\zeta^2 + k_{q1}^2)^{1/2}$, with $q = d, s$; $k_{d2} = 1$, $k_{s2} = c_{d2}/c_{s2}$, $k_{d1} = c_{d2}/c_{d1}$, and $k_{s1} = c_{d2}/c_{s1}$.

The ratios for the transmitted waves to the incident wave at $y = h$ are labelled by the subscripts T_{PP}, T_{PS} (P wave transmits as P or S wave), and the transmitted waves at $y = 0$ are labelled by the superscripts T^{PP}, T^{SP} (transmitted P or S wave transmits as P wave). In addition the ratios for the reflected waves in the layer are denoted by R where superscripts, PP, and subscripts, PP, again relate to the upper and lower interfaces respectively.

Acknowledgements

D. P. Williams and R. V. Craster wish to thank the EPSRC for providing funding via a Research Studentship and an Advanced Fellowship, respectively.

References

1. L. Cagniard, *Réflection et Réfraction des Ondes Séismique Progressives*. Paris: Gauthiers–Villars, Paris (1939). Trans. and rev. by E. A. Flinn and C. H. Dix, *Reflection and Refraction of Progressive Seismic Waves*. New York: McGraw-Hill (1962).
2. A. T. de Hoop, A modification of Cagniard's method for solving seismic pulse problems. *Appl. Sci. Res. B* 8 (1960) 349–356.
3. K. Aki and P. G. Richards, *Quantitative Seismology: Theory and Methods*. San Francisco: W. H. Freeman and Co. (1980).
4. J. Miklowitz, *The Theory of Elastic Waves and Waveguides*. North-Holland (1978).
5. D. P. Williams, Scattering by wave-bearing surfaces under fluid loading. Ph.D. Thesis (University of Nottingham). (1999).
6. F. Hron and B. G. Mikhailenko, Numerical modeling of nongeometrical effects by the Alekseev–Mikhailenko method. *Bull. Seism. Soc. Am.* 71 (1981) 1011–1029.
7. G. R. Mellman and D. V. Helmberger, High-frequency attenuation by a thin high-velocity layer. *Bull. Seism. Soc. Am.* 64 (1974) 1383–1388.
8. G. G. Drijkoningen and C. H. Chapman, Tunneling rays using the Cagniard-de Hoop method. *Bull. Seism. Soc. Am.* 78 (1988) 898–907.
9. G. G. Drijkoningen, Tunneling and the generalized ray method in piecewise homogeneous media. *Geophys. Prosp.* 39 (1991) 757–781.
10. F. Abramovici, H. T. L. Lawrence, and E. R. Kanasewich, The evanescent wave in Cagniard's problem for a line source generating SH waves. *Bull. Seism. Soc. Am.* 79 (1989) 1941–1955.
11. P. R. Gutowski, F. Hron, D. E. Wagner, and S. Treitel, $S^\star$. *Bull. Seism. Soc. Am.* 74 (1984) 61–78.
12. P. F. Daley and F. Hron, High-frequency approximation to the nongeometrical $S^\star$ arrival. *Bull. Seism. Soc. Am.* 73 (1983) 109–123.
13. L. M. Brekhovskikh, *Waves in Layered Media* (2nd ed.). New York: Academic Press (1980).
14. P. D. Einziger and L. B. Felsen, Evanescent waves and complex rays. *IEEE Trans. Antennas Propagat.* AP-30 (1982) 594–605.
15. V. M. Babich and A. P. Kiselev, Non-geometrical waves – are there any? An asymptotic description of some 'non-geometrical' phenomena in seismic wave propagation. *Geophys. J. Int.* 99 (1989) 415–420.
16. R. A. Stephen and S. T. Bolmer, The direct wave root in marine seismology. *Bull. Seism. Soc. Amer.* 75 (1985) 57–67.
17. R. V. Craster, A canonical problem for fluid-solid interfacial wave coupling. *Proc. R. Soc. London A* 452 (1996) 1695–1711.
18. W. L. Roever, T. F. Vining, and E. Strick, Propagation of elastic wave motion from an impulsive source along a fluid/solid interface. *Phil. Trans. Roy. Soc. London A* 251 (1959) 455–523.
19. G. A. D. Briggs, *Acoustic Microscopy*. Monographs on the physics and chemistry of materials: 47, Oxford University Press (1992).
20. Y. H. Pao and R. R. Gajewski, The generalised ray theory and transient responses of layered elastic solids. In: W. P. Mason and R. N. Thurston (eds) *Phys. Acoust. 13*. New York: Academic Press (1977) pp. 183–265.
21. W. M. Ewing, W. S. Jardetzky, and F. Press. *Elastic Waves in Layered Media*. New York: McGraw-Hill (1957).
22. B. L. N. Kennett, *Seismic Wave Propagation in Stratified Media*. Cambridge: CUP (1983).
23. G. Bradfield, Notes on applied science (no. 30). *Use in Industry of Elasticity Measurements in Metals with the Help of Mechanical Vibrations*. London: H.M.S.O. (1964).
24. T. L. Hong and D. V. Helmberger, Generalized ray theory for dipping structure. *Bull. Seism. Soc. Am.* 67 (1977) 995–1008.
25. Y. H. Pao, F. Zeigler, and Y. S. Wang, Acoustic waves generated by a point source in a sloping fluid layer. *J. Acoust. Soc. Am.* 85 (1989) 1414–1426.